INVESTIGATION OF FLOW PATTERNS IN FINITE CYLINDERS

Henrique Fanini Leite, leite05@hotmail.com
Divisão de Pós Graduação, Instituto Tecnológico de Aeronáutica (ITA), 12228-900 São José dos Campos, SP, Brazil
Ana Cristina Avelar, anacristina.avelar@gmail.com
Instituto de Aeronáutica e Espaço (IAE), 12228-900 São José dos Campos, SP, Brazil

Abstract. *The flow patterns over finite cylinders were analyzed experimentally in a subsonic wind tunnel using the techniques of Time Resolved Particle Image Velocimetry (TR-PIV) and Pressure sensitive paint (PSP). The measurements were carried out at the TA-3 wind tunnel, which is a closed circuit wind tunnel with an open test section. The maximum speed through its empty test section is around 38m/s and the turbulence level around 2%. The near wake flow structures, vortex shedding characteristics and surface pressure were investigated for two different aspect ratios, 3 and 6. Tests were performed at speeds from 10m/s to 30m/s, with cylinders with circular and square cross sections. The cylinders diameters are 40mm. For the wind tunnel tests, the cylinders were fixed on a blunt flat plate, creating a boundary layer which interacted with the cylinder wake. The cylinders were also instrumented with pressure taps for comparison with PSP data. The 2D PIV measurements were conducted in vertical and horizontal planes, including regions close to the flat plate, in order to investigate boundary layer interactions. Due to the complexity of the phenomena, the flow was characterized both in terms of average behavior and time-resolved velocity fields. The aim of this work is to analyze the flow patterns around the cylinder and the pressure fluctuations on the wall and flow structure coupling by relating the two-dimensional velocity field with pressure field obtained with PSP.*

Keywords*: PIV method application, Pressure Sensitive Paint, Finite Cylinders, Unsteady Flow, Time Resolved PIV*

1. INTRODUCTION

The flow around a cylinder has been a subject of investigation since the beginning of fluid mechanics. Starting from D'Alembert's Paradox, this type of flow has eluded scientists due to its simple geometry and complex flow structure, which presents many patterns, depending on Reynolds number, ranging from quasi-potential flow for very low Reynolds, to complex vortex-shedding mechanisms at higher Reynolds values. Besides its academic importance, understanding flow behavior around cylinders has many practical applications, such as prediction of drag and buffeting on airplane antennas or vortex induced vibrations in columns and buildings.

Cylinder wake structures are essentially three-dimensional, even for 2D bodies, which is related to vortex deformation (Wang 2015). For finite cylinders, there may be different vortex shedding mechanisms, depending on geometry, which interact in complex ways. The first one is located at the free end of the cylinder, called trailing vortex. If the cylinder is wall-mounted, as in this study, another vortex structure, called necklace or horseshoe vortex, is formed near the wall. This introduces asymmetries, further complicating the flow. The other vortex cell is central, and produces Karman-like vortex structures, depending on Reynolds number. All these structures interact with each other, and it may be difficult to identify them all. For aspect ratios lower than a critical value, which varies between 6 and 8, depending on boundary layer thickness, the central vortex is suppressed by the other two (Levold, 2012; Kawamura et al., 1984). Figure 1 illustrates these vortex structures:

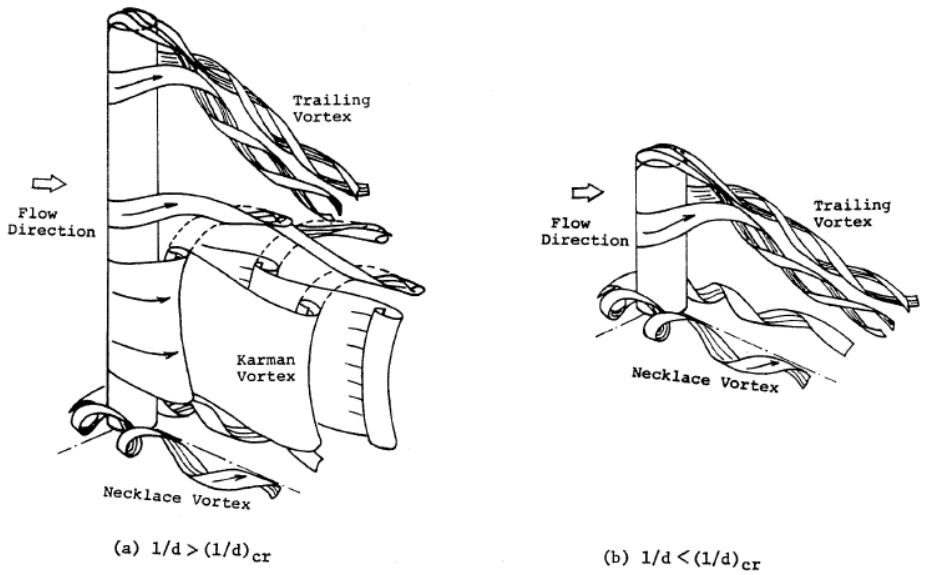

Figure 1. Schematics of the flow around a wall mounted cylinder (Kawamura et al., 1984)

In addition, for very low aspect ratio cylinders, the formation of an arch-vortex structure has been described by Pattenden et al. (2005), as shown in Fig. 2:

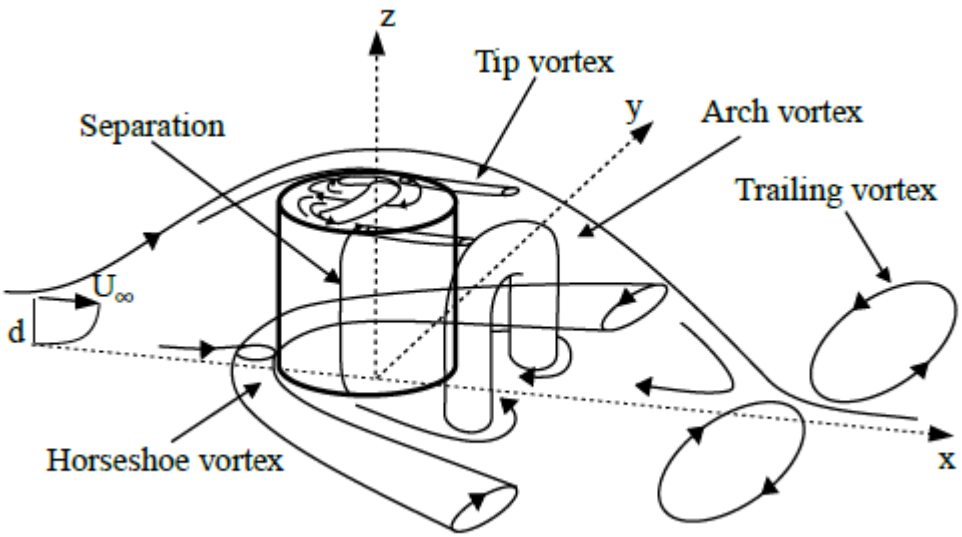

Figure 2. Overview of an arch vortex behind a short wall mounted cylinder (Pattenden et al, 2005)

Although widely studied, the exact mechanisms behind those vortex structures and the interaction patterns between them are still not completely understood. In addition, all those structures are unsteady, shedding vortex at different frequencies, and, as the aspect ratio increases, transition between each of those systems is expected. Although the 2D nature of our PIV measurements presents a serious limitation, mean and time-resolved vertical and horizontal velocity maps are the most direct way of diagnosing the flow, being able to, if not completely define observed structures, provide significant insight into its behavior.

2. METHODOLOGY

The main data source for this investigation were horizontal and vertical 2D velocity fields, measured using time-resolved PIV. In addition, pressure sensitive paint was used to determine the pressure distribution along the cylinders' surface. Reynolds number varied from 27000 to 82000. Measurements were made at three different horizontal planes: near the base, at the middle and near the top. These planes, combined with the vertical plane, can provide important information regarding flow structures, especially for time-averaged fields. Combining each plane's information for instant velocity fields is much more complicated, since measurements were made one plane at a time. If, however, flow structures exhibit a well-defined periodicity, it is possible to relate instant velocity fields too. Measurements were performed at 10m/s, 20m/s and 30m/s. Pressure distribution information was regarded as an auxiliary tool. Low speed PSP measurements are notoriously hard due to low pressure gradients, so the main criteria for choosing experimental conditions was feasibility. Thus, PSP experiments were restricted to flow speed equal or above 30m/s and surfaces which presented significant pressure gradients. In total, 48 different combinations of flow velocity, model type and measuring position were analyzed.

2.1 Wind Tunnel and Model

Tests were carried out at the TA-3 wind tunnel, which is a closed circuit wind tunnel with an open test section. The maximum speed through its empty test section is around 38m/s and the turbulence level is 2%. The open test section facilitated both optical and physical access to the model, allowing for greater flexibility in experiment configuration. Four different cylinder models were tested, two with circular cross section, 40mm diameter and aspect ratios of 3 and 6, and two with square cross section, 40mm side and aspect ratios of 3 and 6. In addition, both AR6 cylinders had pressure taps. Figure 3 gives an schematic of the models and the positioning of the pressure taps, as well as some pictures of the test section, PSP experiment setup and the PIV laser illuminating a model (without tracing particles).

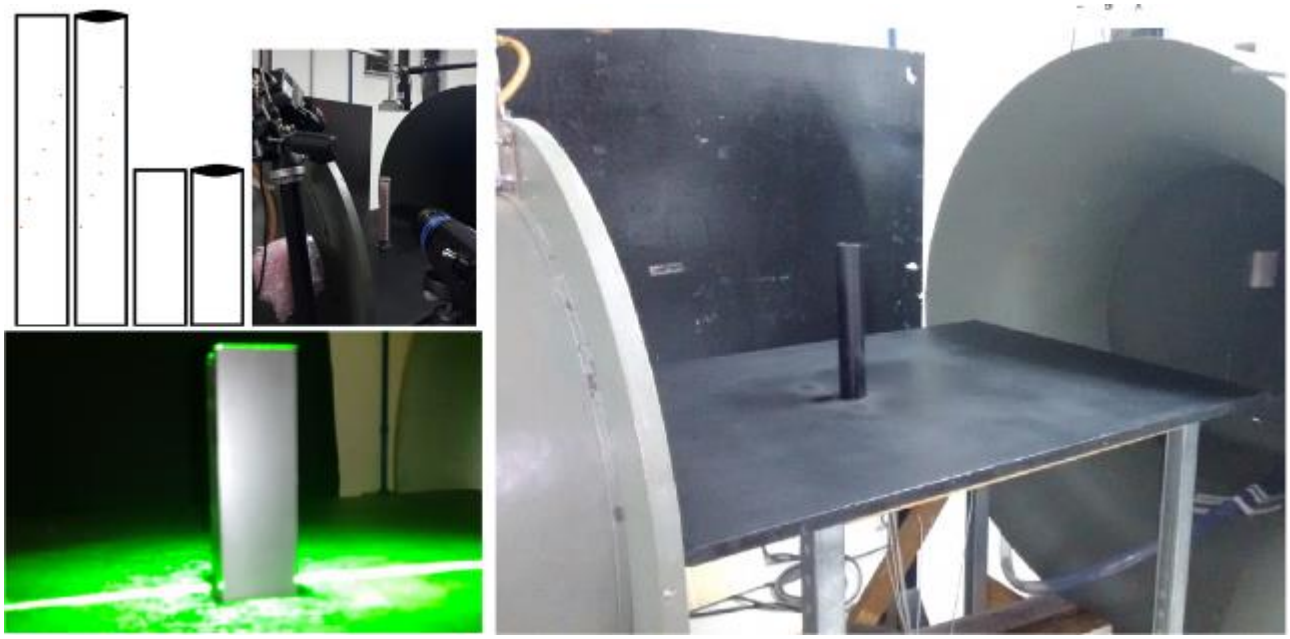

Figure 3. Clockwise, a schematic representation of the cylinder models, a PSP test setup, the tunnel open test section with the AR6 cylinder and the laser beam inciding at a square cylinder model

2.2 Particle Image Velocimetry

Particle image velocimetry is a non-intrusive laser optical measurement technique for research and flow diagnostics based on the optical analysis of tracing particles dispersed through the flow and illuminated by a light source, usually a laser beam. Particle concentration is such that it is possible to identify individual particles, but not track them individually between images. Illumination and acquisition systems are synchronized and able to capture pairs of images within a very short time frame, usually less than 100 microseconds. Velocity is calculated by statistical analysis of image pairs. Figure 4 illustrates a 2D PIV system.

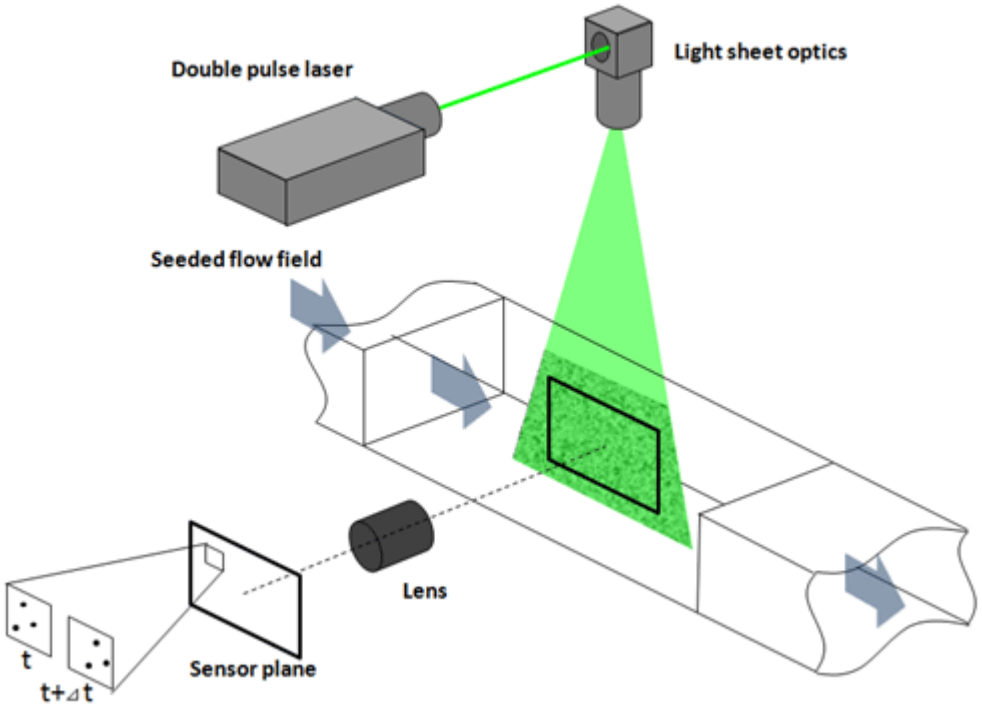

Figure 4. A typical 2D PIV system (http://www.seika-mt.com/product/piv-en/Principle_of_PIV.html)

The light sheet was generated by a Litron pulsed Nd:YLF Laser with 10mJ of energy per cavity, at 1kHz. The whole flow was seeded with poly-ethylene glycol smoke using a high volume liquid seeding generator of Nova Instruments. A 105 mm focal lens with f# equal to 5.6 was used on a SpeedSense 9020 CMOS camera, 1kHz, with full resolution of

1152 x 896 pixels. A light arm from Dantec Dynamics was used to conduct the laser beam, and, consequently, the light sheet to the region of interest. Dynamic Studio software, also from Dantec, was used for data acquisition and processing.

A total of 663 images were taken for each condition. Velocity fields were determined by adaptive correlation, a method with higher computational cost, but which is able to provide better results. It iteratively optimizes the size and shape of each interrogation area to better adapt to local flow gradients and seeding densities, thus optimizing correlation conditions at each interrogation window (Wang, 2015). Window interrogation size was 32x32 pixels and 50% of overlap was considered.

2.3 Pressure Sensitive Paint

Pressure Sensitive Paint is a relatively new technology that has become an important measurement technique in wind tunnels. Compared to pressure taps, PSP allows for lower costs, thanks to a simplified model construction, as well as more versatility, since it provides the pressure distribution over entire models. In addition, it is non-intrusive and has high spatial resolution (Mantel, 2005).

The PSP working principle is the sensitivity of some special dyes, called luminophores, to oxygen. These dyes are dispersed throughout a paint binder, which is sprayed over the model. When excited by a light pulse, the luminophores absorb photons and jump to a higher energy state. To recover its original state, the molecules can either emit a photon back or transfer the absorbed energy to an oxygen molecule, where it becomes vibrational energy. This is called oxygen quenching and is responsible for the dependence of luminecesnce to the partial oxygen pressure. The higher the concentration of oxygen, the lesser the photon emission (Fang, 2010). Pressure is related to luminescence by through a calibration curve based on the Stern-Volmer equation:

$$\frac{I_{ref}}{I} = A + B\frac{p}{p_{ref}} \tag{1}$$

Where I is luminescence intensity and p is pressure. I_{ref} and p_{ref} are the intensity and pressure of a reference image, taken at a known pressure value, usually atmospheric.

Due to the challenging conditions of the experiment, a binary paint was used. Binary paints, also called Biluminophores, are paints that have two types of dye. One of these dyes shows characteristics similar to the ones in conventional PSPs, that is, it is sensitive to pressure and to temperature. The second dye, however, is only sensitive to temperature. It is usual to call the first dye pressure or signal probe and the second one reference probe. In addition, each type of dye emits luminescence in different wavelengths, and it is possible to measure the intensity of the luminescence of each one independently, using optical filters or color cameras. For this type of paint, instead of directly relating luminescence intensity to pressure, the ratio between signal and reference probes is, which reduces errors considerably. The paint, BinaryFIB-400, was provided by Innovative Scientific Solution, ISSI.

The PSP experiment hardware consists of: a PSP-CCD-C color camera, a LM2X LED Lamp of 400nm wavelength, the painted model itself and a commercial laptop for data acquisition. Regarding the camera, filtering is applied on the chip using a standard Bayer filter, which allows binary pressure sensitive paint data to be acquired using a single image acquisition. In the case of Binary FIB, the signal channel is acquired on the red pixels and the reference channel is acquired on the green pixels. In addition, an optical filter was placed on the lens to filter out all sources of light other than paint emission. Communication between the camera and the computer was via an ethernet connection. All camera parameters could be controlled via software, and images were transferred to the computer in real time.

3. RESULTS AND ANALYSIS

Experimental data analysis focused mainly in detecting coherent structures within the flow. Such structures can be identified by many different methods, varying in precision and complexity. For this study, the Fast Fourier Transform (FFT) analysis of time resolved velocity data at a range of positions within the cylinders' wake, the visualization of instant velocity fields and time-averaged velocity fields were deemed sufficient. Such tools are not able to characterize flow structures completely, but provide enough information to determine important variables, such as the vortex shedding frequencies, if there is one.

The time averaged velocity field, or mean velocity field, is helpful to identify coherent structures in an unsteady flow. Although periodic structures, like vortex shedding do not appear in these results, mean wake structures can provide information regarding stationary vortex, as well as help identify vortex-shedding mechanisms. (Levold, 2012). This sort of analysis, however, can also yield similar results to very different behaviors. The square cylinder vortex shedding patterns were markedly different from the regular cylinder, with well-defined shedding frequencies at most regions, whereas the latter did not present such feature. However, time-averaged velocity fields were similar in some cases.

Due to the considerable amount of test cases, experimental data volume was enormous. Therefore, presenting all acquired data would be impractical. Thus, results analysis focused mostly on 20m/s cases, with some results for 10m/s.

Results for other flow velocities were similar, with no remarkable differences. Other than horizontal and vertical velocity components, velocity vector angle and magnitude were analyzed.

3.1 Square Cylinder AR 3

Time-averaged velocity fields for the AR3 square cylinder are presented in Fig. 5. Streamlines are only to facilitate interpretation, and do not provide information regarding velocity magnitude. Color maps represent vorticity ("S"), in (1/s). Scales vary for each image. The gray area represents the cylinder, while the black one represents regions that could not be reached by the laser plane. At the bottom right, the 20m/s reference vector is represented:

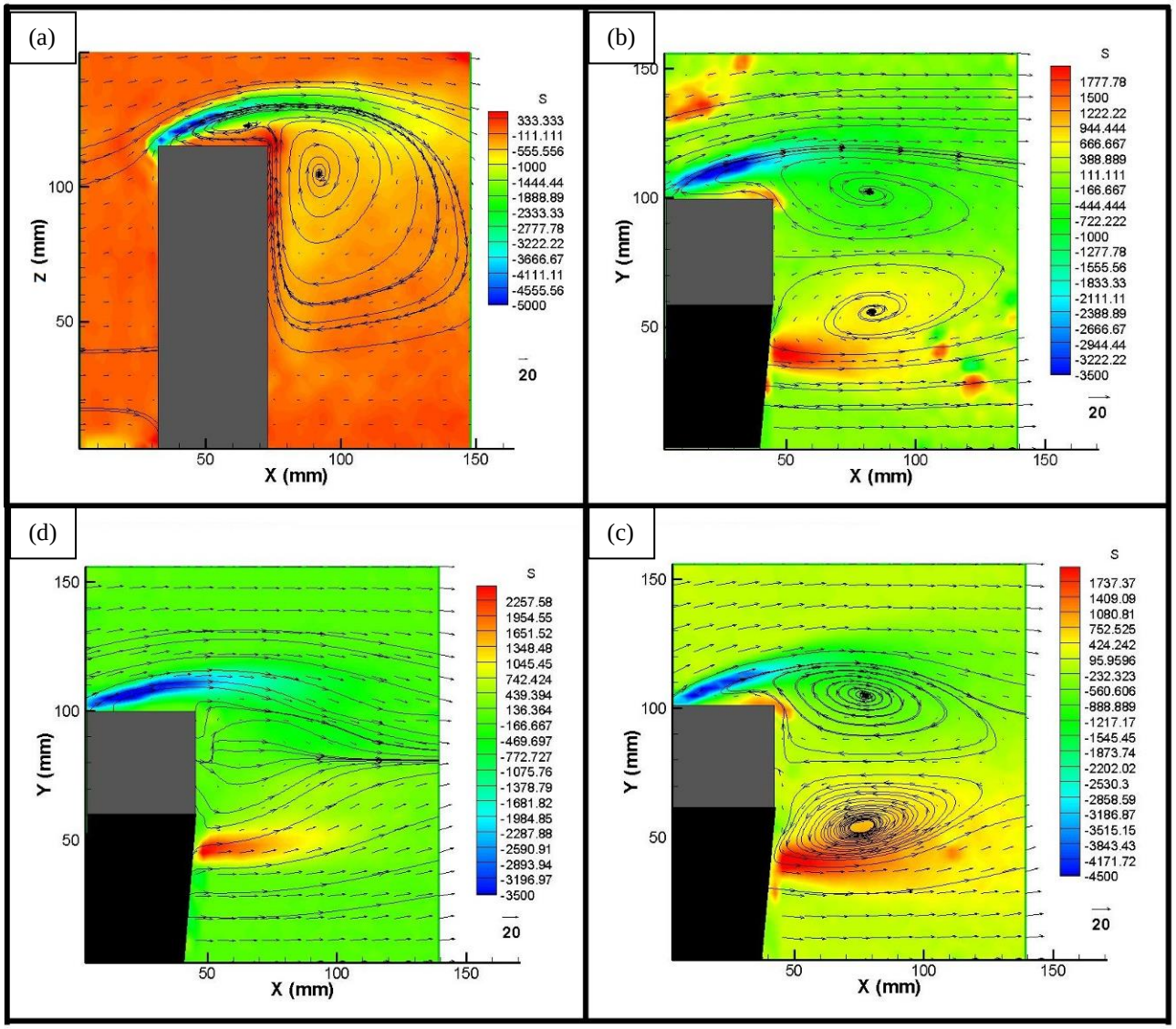

Figure 5. Time-averaged velocity fields and vorticity maps for: (a) vertical plane; (b) bottom horizontal plane (z/h=0.3); (c) middle horizontal plane (60mm, or z/h=0.5) and (d) tip.

None of the flow structures represented in Fig. 5 are visible within instantaneous velocity fields, which can be seen in Fig. 6. Of the vortex represented in Fig. 5, only the arch vortex, visible on the vertical plane image is stationary. That does not mean velocity fields will be exactly as shown in it, but that this structure does not shed vortexes. Another important information is that horizontal vortex core positions do not change considerably from the middle to the bottom plane. This suggests that the influence of the tip-induced downwash is equally felt at both positions, or that the horizontal flow mechanisms predominate over it. At the top plane, no vortex structures can be noticed, which suggests that the main flow and the vertical arch vortex predominate. Overall, the mean velocity fields suggest a flow structure similar to the one illustrated in Fig. 2. In addition, a separation bubble could be detected at the tip, which is induced by the cylinder's sharp edge.

The horseshoe vortex and the tip vortex described in Fig. 2 could not be detected, since they would induce vertical velocity variations at the edges of the cylinder, undetectable by the 2D PIV at horizontal planes, and far from the vertical plane shown in Fig. 5. At 10m/s and 30m/s the same sorts of flow structures were detected, with some variations in core position.

Figure 6 presents instant velocity fields both at the vertical plane, Fig. 6a, and bottom horizontal plane, Fig. 6b. At the upper left corners of the images, measured velocities could not be properly measured due to lack of illumination. Fortunately, these regions are not of interest to the current study.

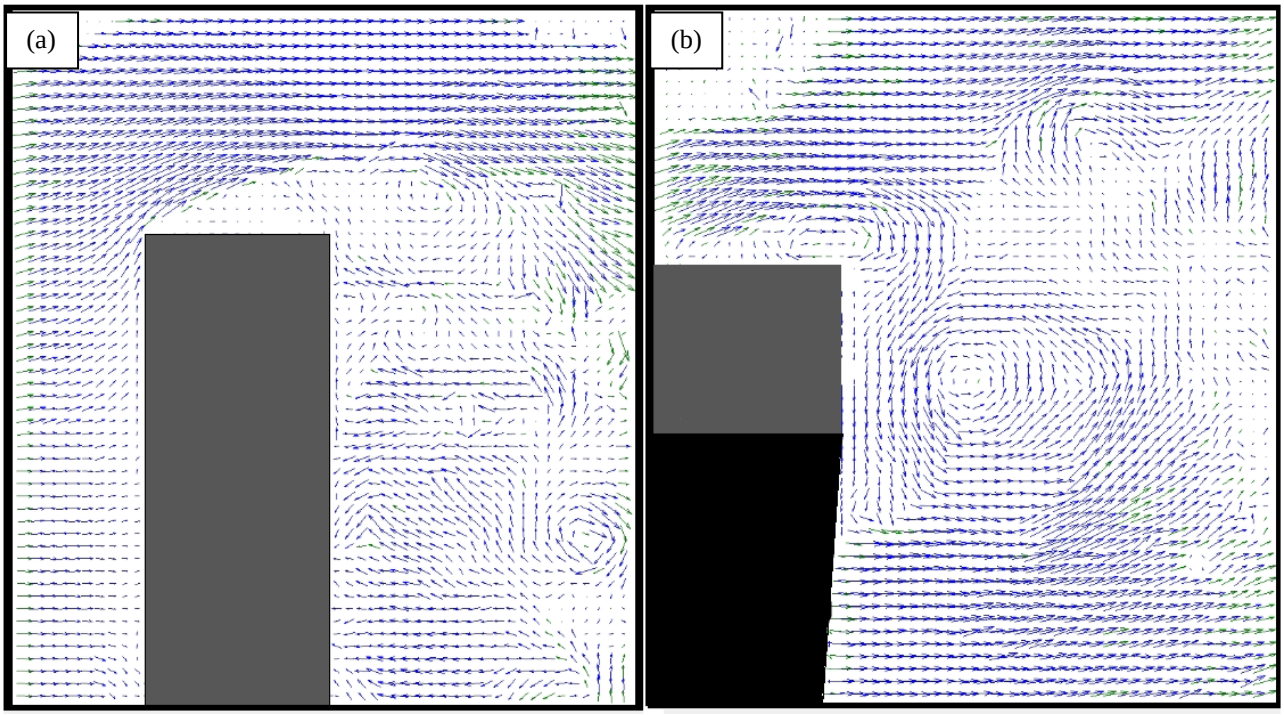

Figure 6. Instant Velocity fields for an AR3 square section cylinder, left: (a) vertical plane, right: (b) bottom horizontal plane

Both images in Fig. 6 present a series of vortexes. At the bottom horizontal plane, it is possible to see a Karman-like vortex structure; with one vortex moving downstream while another one starts forming at the upper side of the cylinder. This image illustrates the role of flow detachment in spanwise vortex shedding: each vortex begins as a recirculation bubble, growing and becoming a vortex in a continuous process. Depending on the cylinder's aspect ratio, as well as boundary layer thickness and incoming turbulence intensity, symmetrical or anti-symmetrical spanwise shedding mechanisms can predominate, with symmetrical ones predominating at aspect ratios below a certain critical value, which varies between 2 and 7 (Wang, 2012). Surprisingly, the image in Fig.6a indicates an anti-symmetrical type of vortex shedding, similar to 2D cylinders. Observation of a film-like succession of instant-velocity fields suggests both symmetrical and anti-symmetrical vortex shedding mechanisms are present, both predominating at different moments. No pattern could be devised by simple observation, however. Comparing the instantaneous velocity fields with the time-averaged ones it becomes clear that mean flow representation does not correspond to the actual flow, useful only as a tool to understand the flow patterns behavior.

FFT analysis indicates that, for the square AR3 cylinder, both horizontal U and V velocity components, as well as the vector angle, oscillate at frequencies ranging from 50.54Hz to 51.51Hz, resulting in Strouhal numbers from 0.101 to 0.103, depending on the data point. These results match both experimental data and numerical simulations very closely (Bourgeois et al., 2011; Wang et al., 2011). In addition, the vector angle at the bottom plane presents a secondary frequency peak at Sr = 0.202 (101.3Hz), which is barely visible in Fig.7. This secondary frequency is a natural harmonic of the main one. Another important information regarding the horizontal plane is that the 0Hz component grows in magnitude as z/h increases, indicating that the closer to the cylinder's free edge, the stronger the predominance of the main flow velocity is, since 0Hz component means a constant velocity component. At z/h = 1, the 51Hz component is only visible at the analysis of the vector angle, being completely dominated by the main flow velocity both for U and V velocity components. Since this analysis was made to a wide range of data points, it is possible that some points unaffected by the cylinder's wake presented extremely high 0Hz components, which masked important secondary components of other data points due to scaling factors. This observation is supported by the fact that the "y" axis arbitrary magnitude grows considerably with the increase of z/h , with the exception of the vector angle, the only one in which non-zero frequencies components remain visible. The reduction of such components importance, however

is not simply an effect of scaling, since even at the vector angle analysis, its FFT absolute value diminishes ("y" axis scale factor is lower for the vector angle *z/h* = 1 case).

In view of scaling issues, "y" axis range was limited for the vertical plane FFT. This allowed the detection of frequencies which otherwise would not be visible. Therefore, in interpreting such figure, one must bear in mind that the detected frequency components are very small when compared to the 0Hz component, even for the vector angle case. Thus, no coherent vortex emission patterns were detected on the vertical plane, confirming - of at least strongly supporting - the hypothesis that the arch vortex detected by time-averaged velocity field analysis is stationary. The secondary frequency peak is slightly spread out, but its main frequency is 109.6Hz. The data point responsible for this peak is located near the bottom plane, indicating that this detected frequency probably has to do with interactions between spanwise vortex shedding and the tip induced downwash. Data points located at higher z/h values do not present any FFT peaks, further supporting the hypothesis of increased downwash predominance at higher z/h values.

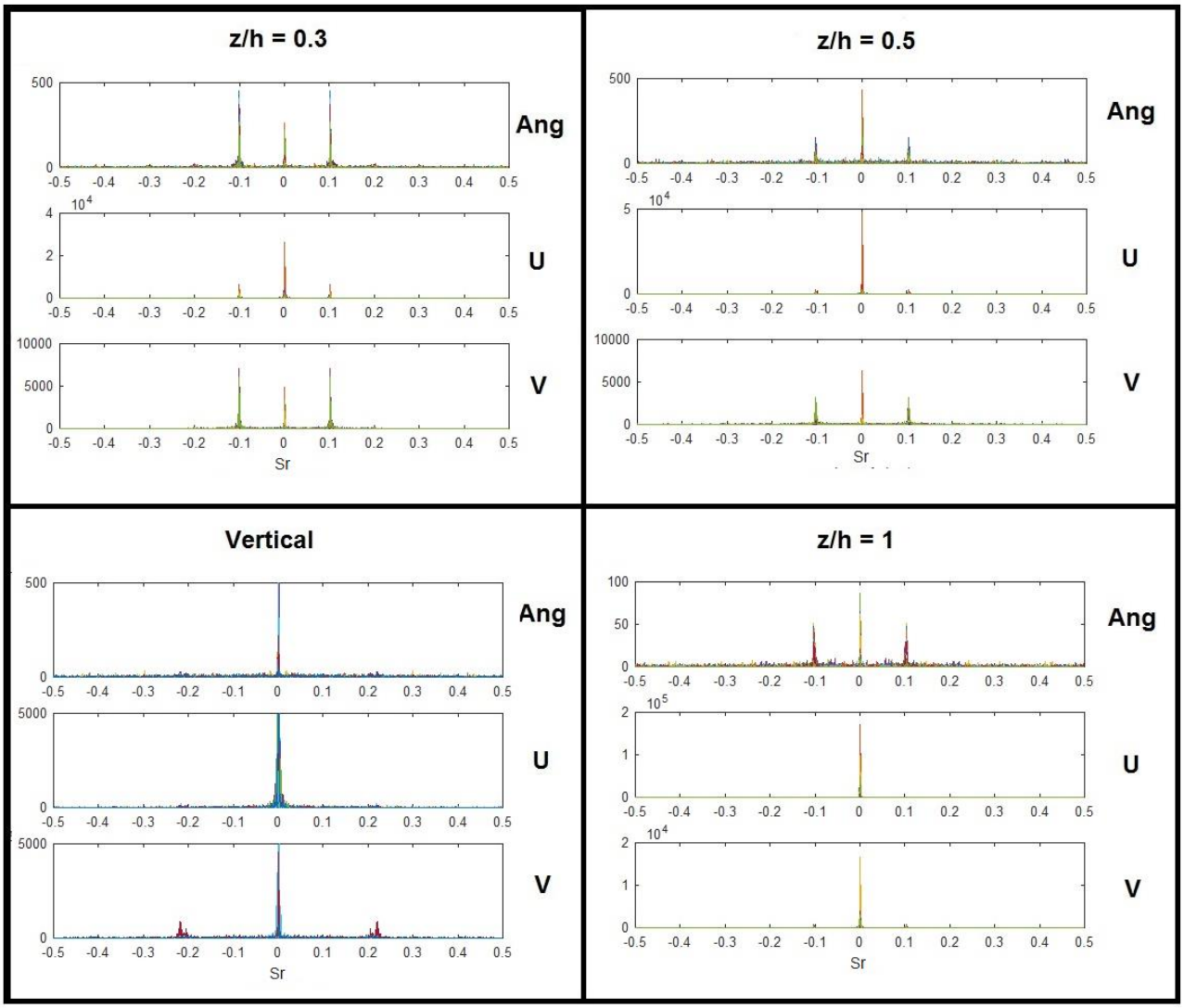

Figure 7. FFT analysis of vector angle, horizontal and vertical velocity components. Clockwise: bottom plane, middle plane, top plane and vertical plane.

3.2 Square Cylinder AR 6

Time-averaged velocity results for the AR6 square cylinder, presented in Fig. 8, were close to the AR3 case. The arch vortex core moved a few millimeters upstream, while horizontal vortex cores moved downstream, remaining at almost the same position both at the middle and bottom horizontal planes. Due to the increased cylinder height, the tip-induced downwash has even less influence on these planes. The middle plane, for instance, is 120mm distant from the tip, while in the AR3 case, this distance was only 60mm. The image of flow field in the vertical plane was not able to capture the whole cylinder, showing only its upper half. Vorticity values remained similar to the previous case as well. Again, both anti-symmetrical and symmetrical vortex structures were detected at the instant-velocity fields, with longer periods of symmetrical vortex shedding when compared to the AR3 case, while anti-symmetrical vortex still

predominated most of the time. This behavior seems at odds with what has been described by other researchers, since lower aspect ratios were shown to favor the symmetrical vortex shedding mechanism. Our observations, however, were based on velocity fields taken at a very short time period (about 1,3s). In addition, many variables affect such mechanisms. Stronger statistical methods, such as Proper Orthogonal Decomposition (POD) might be able to elucidate this phenomenon.

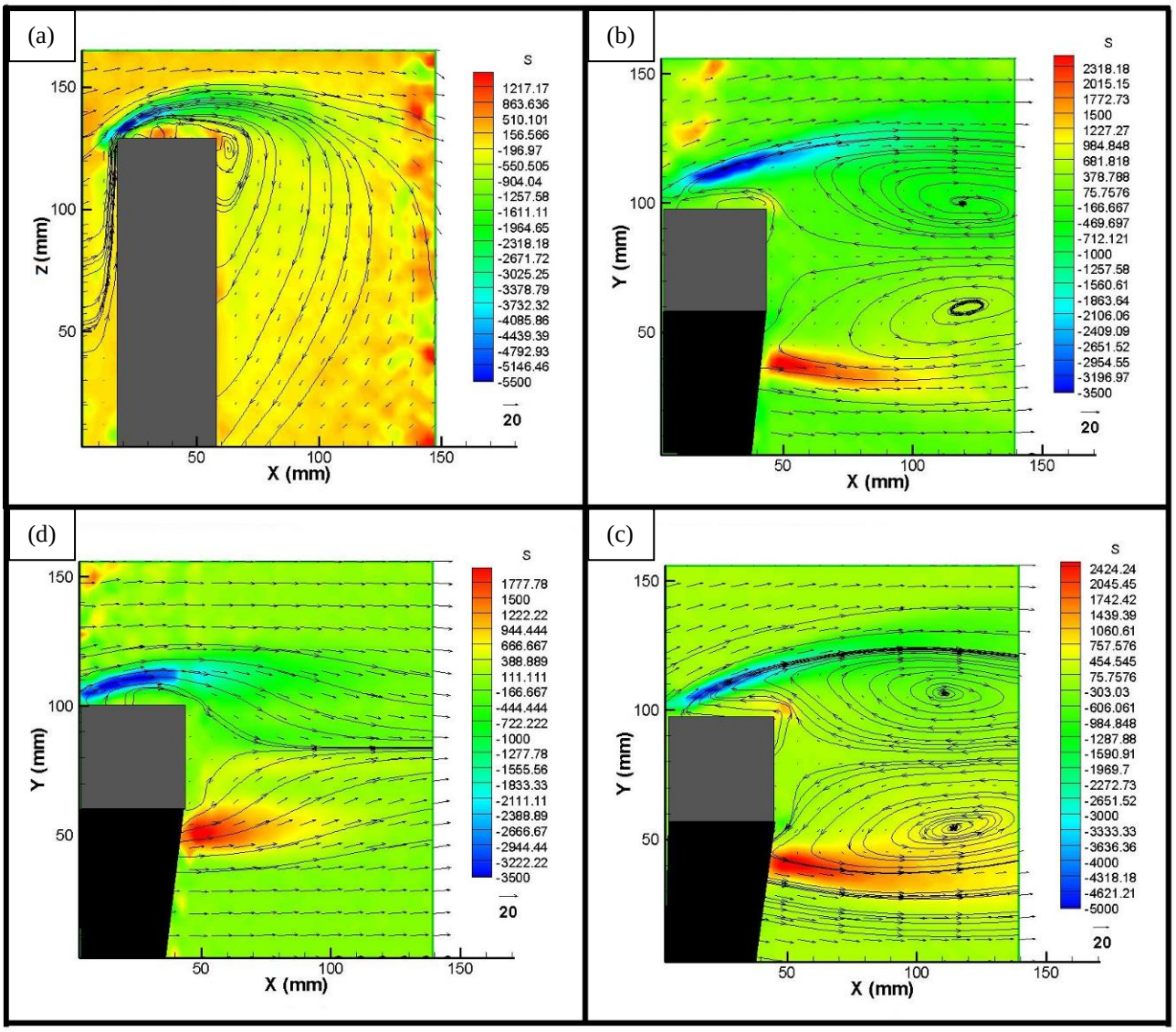

Figure 8. AR6 square cylinder time-averaged velocity fields and vorticity maps for: (a) vertical plane; (b) bottom horizontal plane (0.15 z/h); (c) middle horizontal plane (120mm, or 0,5 z/h) and (d) tip. Only the cylinder's upper half was captured by the vertical plane image.

FFT analysis, presented in Fig. 9, indicates a Strouhal number of 0.106, very close to the AR3 case. Since Reynolds Number was the same, no important variations on the Strouhal number were expected. As z/h increases, the FFT peaks disappear, except at $Sr = 0$, and, contrary to the AR3 case, no peaks were detected at the vertical plane. It should be noted, however, that the PIV image for the AR6 case captured only the upper half of the cylinder, while the only data points of the vertical plane that presented a defined Strouhal number for the AR3 case were the ones near the bottom plane. Therefore, it cannot be ruled out that similar peaks could have been detected for the AR6 case had data points from the lower half of the cylinder been analyzed.

Both cases present an interesting behavior: the lower the value of z/h, the stronger the non-zero FFT peaks. Such phenomenon cannot be completely explained by a lower interference of the tip-induced downwash, since the absolute distance between the cylinder's free end and the AR6 cylinder middle plane is greater than the distance between the free end and the AR3 cylinder bottom plane, while the latter shows better defined FFT peaks. Of course, the flow is different for each case, as seen when comparing Fig. 5 and Fig. 8: at the AR6 middle plane, the vertical plane flow is diagonal, going to the bottom left. In comparison, the vertical plane flow at the bottom of the AR3 cylinder is mostly horizontal, to the left. Velocity magnitude is similar, despite the difference in direction. The remaining factor playing an important

part in flow dynamics is the proximity to the ground, which accounts for the apparent contradiction: the AR3 bottom plane is much closer to the surface than the AR6 middle plane.

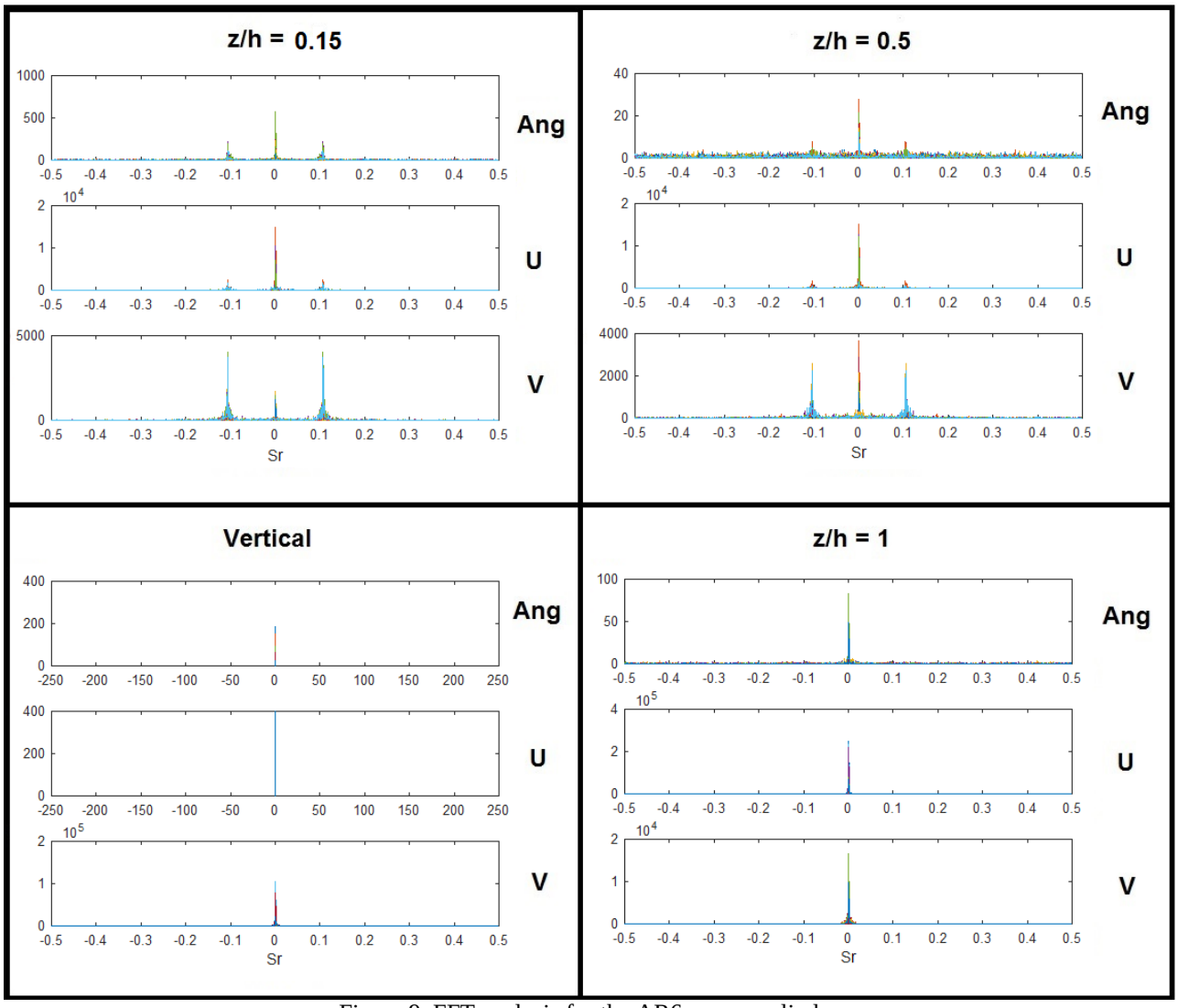

Figure 9. FFT analysis for the AR6 square cylinder.

3.3 Regular Cylinder AR3

The same experimental conditions to which the square cylinders were subjected were applied to the regular cylinders. In this paper, however, only results obtained at a main flow velocity of 10m/s will be presented. In comparison with the square cylinders, adverse pressure gradients are weaker for regular cylinders, since the geometry does not change abruptly. Flow detachment occurs nevertheless, but its effects are less predominant. Thus, Karmann-like vortex shedding is not as evident in low aspect ratio cylinders, with strong predominance of other flow mechanisms. Experiments performed by Kawamura et al. (1984) at similar Reynolds have shown the critical slenderness ratio to vary between 6 and 8, depending on boundary layer thickness. At lower slenderness values, no defined vortex shedding frequency is expected. In view of this, the results presented in Fig. 10, which represent the FFT analysis for the AR3 regular cylinder, are surprising. Although less defined than the ones detected on the square cylinders wake, FFT analysis clearly indicates a peak at Sr = 0.1793, corresponding to a frequency of 44.825 Hz. The Strouhal number value for a 2D cylinder at *Re* = 27000 is close to 0.19, indicating the possibility that the detected frequency might be related to Karmann-like vortex shedding. An important remark is that a few data points, all of them within the cylinder's wake, presented such peak, reducing the odds of a possible mistake. For the AR6 cylinder, no peaks were detected, again presenting an unexpected behavior, since a higher slenderness ratio was supposed to reduce the predominance of 3D effects. A possible explanation is that the Karman vortex shedding region was located between the bottom plane and the middle plane *(z/h* = 0.15 and 0.5, respectively) and thus was not detected.

Further research is necessary to properly elucidate flow behavior at these conditions, since results were contradictory and did not match well-established references. In special, more sophisticated statistical tools can provide crucial information, especially Proper Orthogonal Decomposition and Power Spectral Analysis

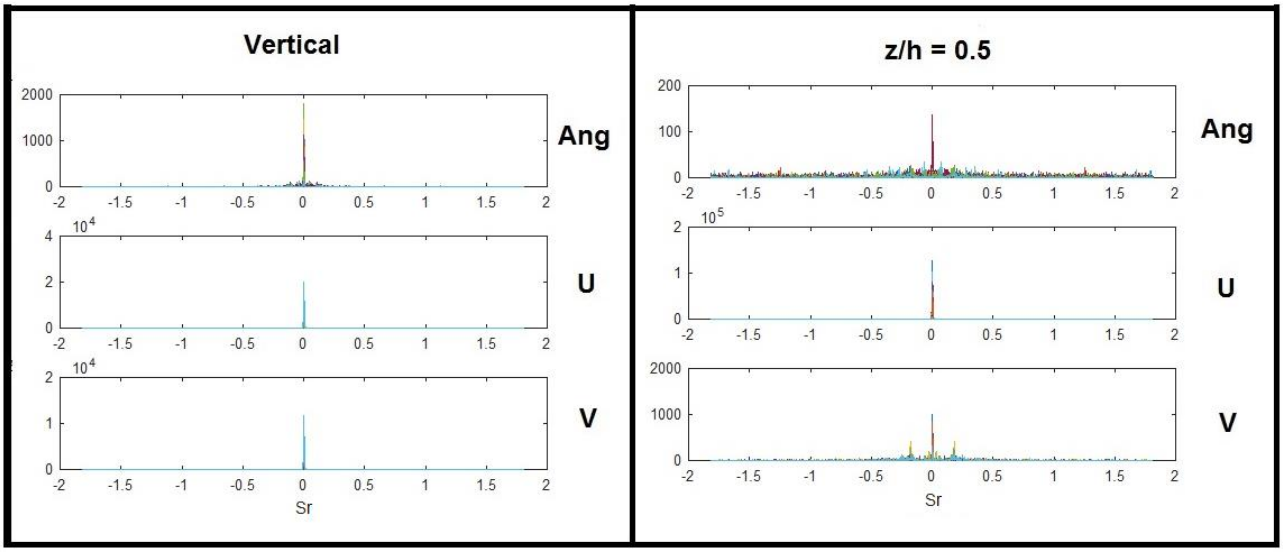

Figure 10. FFT analysis for the AR3 regular cylinder.

Time-averaged flow analysis clearly reveals the presence of an arch vortex behind the cylinder, but does not support the type of structure illustrated in Fig. 2. Horizontal plane mean flow does not reveal two counter rotating vortex, but a dipole-like point located around 2.5 diameters from the cylinder. This structure does not correspond to the actual flow – dipoles are a theoretical construct used to model fluid dynamics – and is simply a result of the averaging of all the instant-velocity fields. Nevertheless, this result allows us to conclude that the vortex shedding structure is not Karmann-like, since such structure would result in the classical two-vortex mean flow seen in the square cylinder case. It is, in fact, representative of predominantly symmetrical vortex shedding, similar to what one would find at a time-averaged wake of a sphere.

Therefore, results presented in Fig. 11 indicate a strong influence of 3D structures in the flow. Contrary to what the FFT analysis suggested, the Strouhal number peak was not due to Karmann vortex structures, but due to symmetrical vortex shedding.

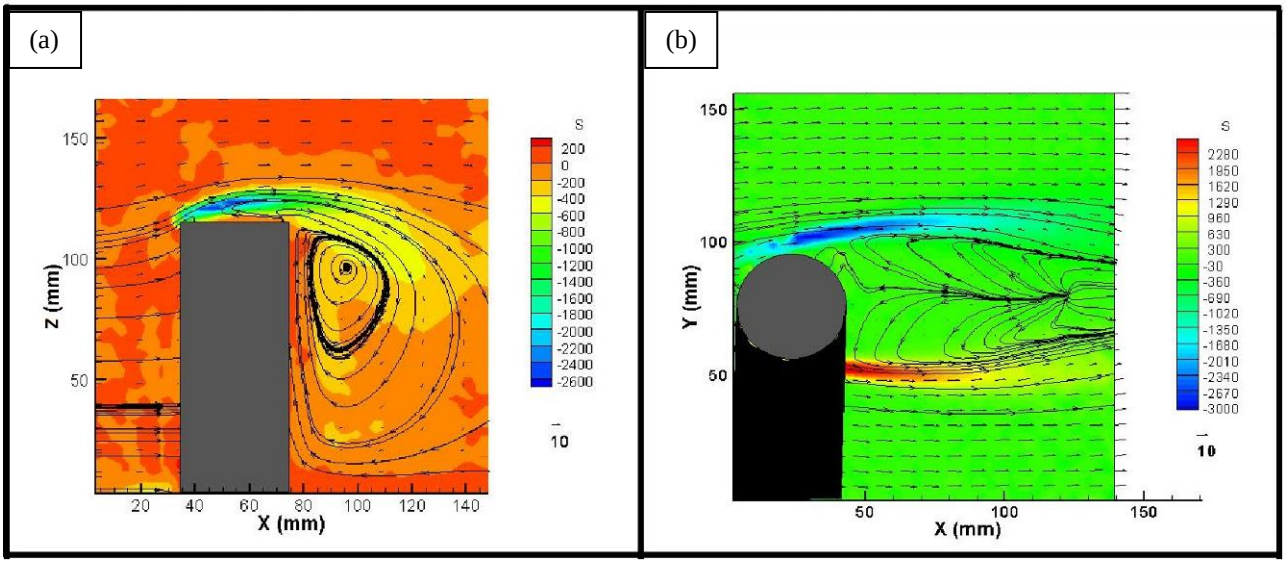

Figure 11. Time-averaged velocity fields and vorticity maps at: (a) vertical and (b) middle horizontal planes for a cylinder of a slenderness ratio of three.

3.4 Regular Cylinder AR 6

As stated in the previous section, FFT analysis did not detect any frequency peak, agreeing with previous studies (Kawamura et al. 1984). This leaves time-averaged and instant velocity fields as the only information sources for this condition. Figure 12 presents the time-averaged flow at all measured planes. Unfortunately, with the exception of the vertical plane, most structures were not completely captured, having formed downstream of the image frame. In comparison to the square cylinders, the wake is "thinner" and vortex cores are downstream.

In Fig. 12b, a vortex core is visible, which suggests that time-averaged flow for the AR6 cylinder would present traditional counter rotating vortex. There is, however, a subtle difference between the flow characterized in Fig. 12 and the ones in Fig. 8 and Fig. 5: while streamlines diverge from the vortex core in the latter two, in Fig. 12 streamlines "enter" the vortex core. Thus, further downstream there probably is a dipole-like point from which those streamlines originate. The physical interpretation of this phenomenon is elusive, but it might be the result of a combination of different vortex shedding mechanisms which co-existed in the flow. Such hypothesis is highly speculative, especially given the incomplete nature of acquired data. Another noticeable change is the shape of the vertical arch vortex, in Fig. 12a, which became elongated, while its core moved slightly upstream. As in the AR6 square cylinder case, only the upper half of the cylinder was captured. Finally, vorticity were slightly lower than the AR3 case, but followed the same trends observed in all cases.

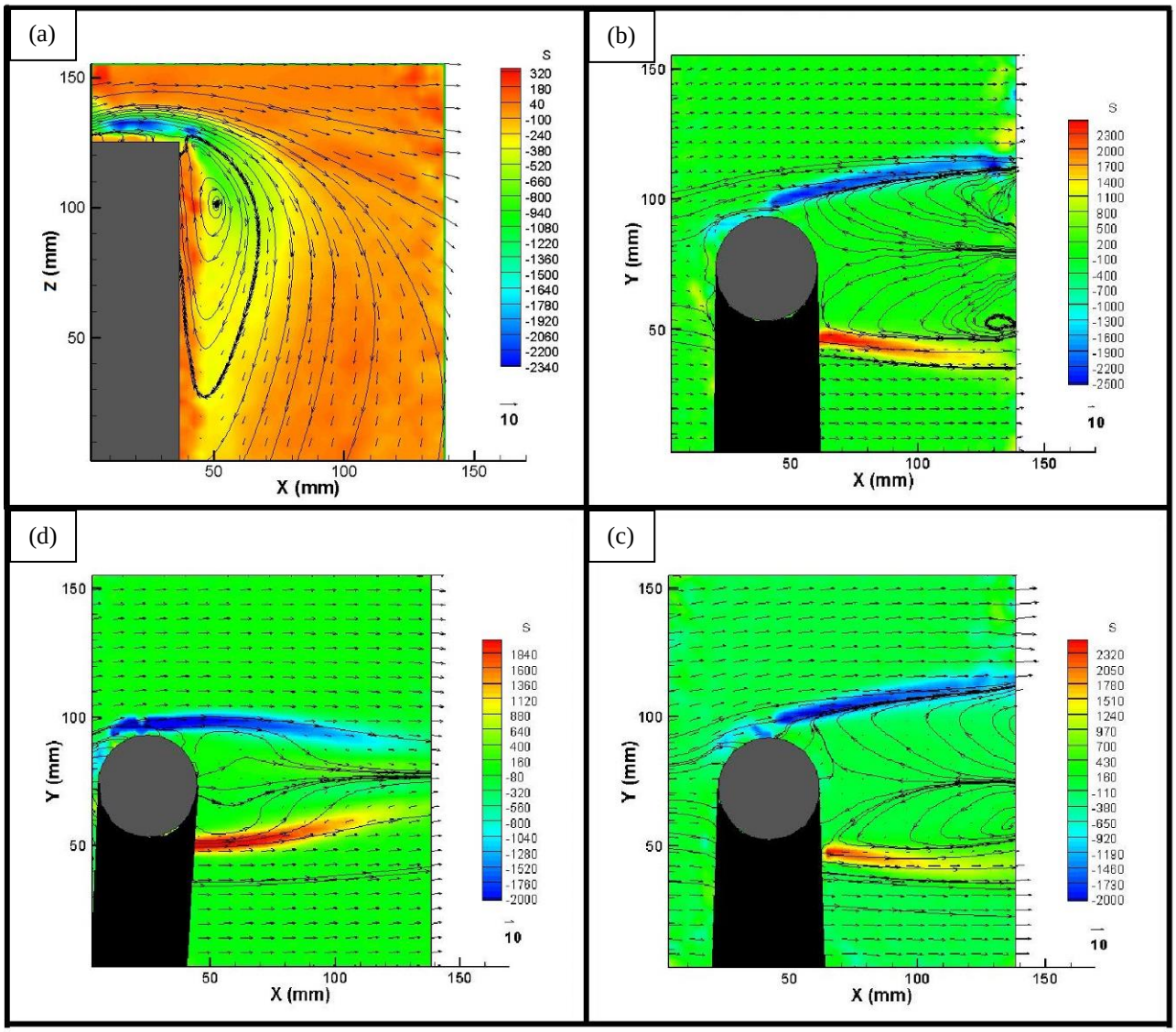

Figure 12. AR6 regular cylinder time-averaged velocity fields and vorticity maps for: (a) vertical plane; (b) bottom horizontal plane (0.15 z/h); (c) middle horizontal plane (120mm, or 0,5 z/h) and (d) tip. Only the cylinder's upper half was captured by the vertical plane image.

3.5 Pressure Sensitive Paint

Even at the highest velocity condition, pressure gradients were lower than 1000Pa, rendering PSP testing extremely challenging. BinaryFIB luminescence response is 0.7% per kPa, which resulted in a very low signal to noise ratio (SNR) and required intensive signal filtering to determine the actual pressure distribution. In addition, vortex shedding caused the models to vibrate, complicating image alignment. In conventional PSP, it is usual to average a series of images to reduce noise, but in this case this had the effect of "blurring" the images. Even though image markers were extensively used for alignment, this issue could not be completely resolved. Thus, although PSP data agreed with pressure tap data, it did not present the required precision to contribute to flow diagnostics. Figure 13 presents pressure distribution results for a front side of the square cylinder at 45° and flow velocity of 30m/s, the best-case test condition. As one may see, pressure behavior was correctly determined, but precision was not sufficient for deeper analysis.

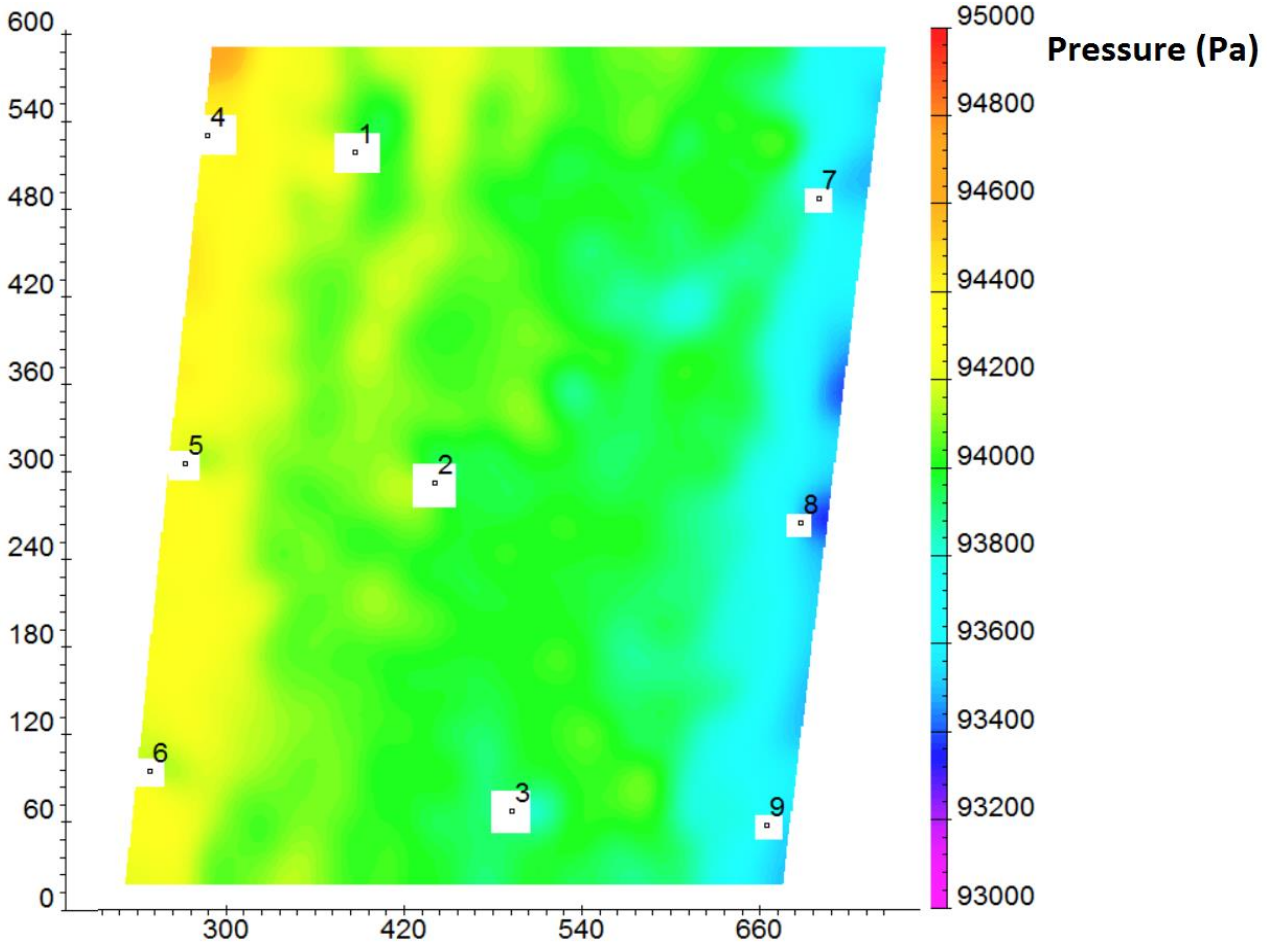

Figure 13. Pressure distribution at the front side of a square cylinder facing the flow at 45°, U=30m/s.

4. CONCLUSION

The flow patterns over square and regular cylinders with aspect ratios of 3 and 6 were analyzed in four planes: vertical, bottom horizontal, middle horizontal and tip. Results for the square cylinders were markedly different from the results for circular ones, mainly due to the predominance of karmann-like vortex shedding, albeit strongly influenced by both the tip induced downwash and boundary layer interactions. In comparison with the regular cylinders, negative pressure gradients were stronger, and, thus, also flow detachment, a direct consequence of the sharp corners. From this comparison, it became clear that traditional vortex shedding is strongly related to flow detachment dynamics. In addition, the detected vortex shedding had a well-defined frequency, which matched other experimental results. Flow dynamics did not vary considerably with an increase in aspect ratio.

For the regular cylinders, only a single FFT analysis indicated a peak, which was not very pronounced. This peak, however, was close to what is observed in 2D cylinder wakes. Time averaged flow analysis suggested a stronger role for symmetrical vortex shedding, although this cannot be confirmed without the use of more sophisticated statistical methods. Finally, an increase in aspect ratio did not result in considerable changes, although no frequency peak could be detected for the AR6 case.

5. ACKNOWLEDGEMENTS

The Author thanks the Conselho Nacional de Pesquisa e Desenvolvimento (CNPq) for the financial support through the grants: 402233/2013-1, 308829/2015-8 – DT and the process 381094/2016-2.

6. REFERENCES

Bourgeois, J. A., Sattari, P., Matinuzzi, R. J., 2011. "Alternating half-loop shedding in the turbulent wake of a finite surface-mounted square cylinder with a thin boundary layer". Physics of Fluids, Vol. 23, Paper no. 095101-1.

Fang, S., 2010. "Application of fast-responding pressure-sensitive paint to a hemispherical dome in unsteady transonic flow". Master of Science Degree thesis, The Ohio State University, Columbus;

Kawamura, T., Hiwada, M., Hibino, T., Mabuchi, I., Kumada, M., 1984. "Flow around a finite circular cylinder on a flat plate". Bulletin of JSME, Vol. 27, No. 232, pp. 2142 – 2151.

Levold, P., 2012. "Viscous flow around finite length circular cylinder". Master of Science Degree thesis, Norwegian University of Science and Technology, Trondhein, Norway.

Mantel, J., 2005. "Understanding and improving pressure sensitive paint based on luminescence decay". Master of Science Degree thesis, Delft University of Technology, Delft;

Pattenden, R. J., Turnok, S. R., Zhang, X., 2005. "Measurements of the flow over a low aspect ratio cylinder mounted on a ground plane". Experiments in Fluids, Vol. 39, No. 1, pp. 10-21.

Wang, G., 2015. "PIV experiment and CFD simulation of flow around cylinder". Master of Science Degree thesis, University of Texas, Austin, Texas, USA.

Wang, H., 2012. "POD analysis of the finite-length square cylinder wake". In proceedings of The Seventh International Colloquium on Bluff Body Aerodynamics and Applications (BBAA7). Shanghai, China

Wang, Y. Q., Jackson, P., Sui, J., 2011. "Simulation of flow around a surface-mounted square-section cylinder of aspect ratio four". in proceedings of the 20th Annual Conference of the CFD Society of Canada. Canmore, AB, Canada.

7. RESPONSIBILITY NOTICE

The authors are the only responsible for the printed material included in this paper.